Corrosion behavior of the friction-stir-welded joints of 2A14-T6 aluminum alloy

Hai-long Qin[1], *Hua Zhang*[2], *Da-tong Sun*[3], *and Qian-yu Zhuang*[1]

1) School of Materials Science and Engineering, University of Science and Technology Beijing, Beijing 100083, China

2) The Welding Institute, Cambridge CB21 6AL, UK

3) Chongqing Changan Automobile Co. Ltd., Chongqing 400023, China

Abstract: The corrosion behavior of friction-stir-welded 2A14-T6 aluminum alloy was investigated by immersion testing in immersion exfoliation corrosion (EXCO) solution. Electrochemical measurements (open circuit potential, potentiodynamic polarization curves, and electrochemical impedance spectroscopy), scanning electron microscopy, and energy dispersive spectroscopy were employed for analyzing the corrosion mechanism. The results show that, compared to the base material, the corrosion resistance of the friction-stir welds is greatly improved, and the weld nugget has the highest corrosion resistance. The pitting susceptibility originates from the edge of Al–Cu–Fe–Mn–Si phase particles as the cathode compared to the matrix due to their high self-corrosion potential. No corrosion activity is observed around the θ phase (Al_2Cu) after 2 h of immersion in EXCO solution.

Keywords: aluminum alloys; friction stir welding; joints; corrosion; *in-situ* observation

1. Introduction

2A14 aluminum alloy is widely used in aircraft and aerospace applications because of its high strength-to-weight ratio and good formability. However, it is difficult to join this alloy by traditional fusion welding techniques due to the high susceptibility to cracking and porosity and the apparent mechanical property degradation during welding. Friction-stir welding (FSW), a new solid state welding technique, was invented by The Welding Institute (TWI) in 1991 [1]. This technique improves the quality of the joints due to the presence of fine equiaxed grains in the welds [2–6].

The corrosion resistance of FSW joints is different from the base material (BM). In the past decade, the studies of corrosion behavior of friction-stir-welded aluminum alloy have focused on general corrosion behavior [7–14], stress corrosion cracking (SCC) [15–17], and improvement of corrosion resistance [18–23]. For heat-treatable alloys such as AA2024, decreases in corrosion resistance in the weld region are common [9–11], however, the AA2219 alloy exhibits the improved corrosion resistance in its welds [12–13,17,24–26]. Paglia and Buchheit [6] and Srinivasan *et al.* [16] found that the general corrosion behavior of weld nugget was superior to that of the parent material for AA2219-T87 aluminum alloy. However, this previous work focused mainly on the corrosion behavior of welds in NaCl solution; only a few studies have focused on pitting and intergranular corrosion of FSW joints in immersion exfoliation corrosion (EXCO) solution.

Second phase particles are known to have an important influence on the corrosion behavior of aluminum alloys [27–28]. Two major precipitates (Al_2Cu (θ) and Al_2CuMg (S) phases) are present in the 2xxx series of Cu-containing aluminum alloys, leading to pitting and intergranular corrosion. The θ phase acts as the cathode and accelerates the dissolution of the adjacent matrix [12–13,24]. The S phase acts as the anode and can resist corrosion attack in early stages, but will lead to the dissolution of the adjacent matrix with increasing immersion time [11,29–30].

The θ phase and Al–Cu–Fe–Mn–(Si) are the major precipitates in 2A14 aluminum alloy, and the composition varies greatly [28,30]. The Al–Cu–Fe–Mn–(Si) phase particles

Ⓐ Springer

act as the cathode due to their high self-corrosion potential compared with the matrix [30–31]. In the studies of Shao *et al.* [30], the S phase played an important role in the corrosion process of 2024-T3 aluminum alloy, and no pitting corrosion occurred on the Al–Cu–Fe–Mn phase particles. Although the Al–Cu–Fe–Mn phase particles act as the cathode, corrosion attack is also found on these particles with the prolonged immersion time in NaCl solution [30]. However, the corrosion behavior of second phase particles in FSW 2A14 aluminum alloy in EXCO solution has not been reported.

In the present work, the corrosion behavior of FSW joints of 2A14-T6 aluminum alloy was investigated by EXCO solution immersing testing, and the development of corrosion was studied by *in-situ* observation. The corrosion behavior and mechanism were studied by electrochemistry measurements, scanning electron microscopy (SEM), and energy dispersive spectroscopy (EDS).

2. Experimental

2.1. Materials and solutions

A 7-mm thick 2A14 aluminum alloy plate in T6 temper condition was used in the present work; its chemical composition is shown in Table 1. The joints were manufactured by an FSW machine at a travel speed of 50 mm/min and a rotation speed of 800 r/min at Capital Aerospace Machinery Company. The tilt angle of FSW tool was 3° with respect to the vertical direction.

Table 1. Chemical composition of 2A14-T6 aluminum alloy

wt%

Si	Fe	Cu	Mn	Mg	Zn	Ti	Al
0.6–1.2	0.7	4.4	0.4–1.0	0.4–0.8	0.3	0.15	Bal.

One FSW specimen of about 30 mm × 10 mm × 7 mm was sectioned perpendicularly to the welding direction from the joints. The cross section of specimen was ground by silicon carbide papers in a row to 2000# and then polished with diamond paste to a 1-µm finish. The specimen was etched by Keller's reagent (1 mL HF, 1.5 mL HCl, 2.5 mL HNO$_3$, and 95 mL H$_2$O) for microstructural examination.

All solutions in this study were prepared according to the ASTM G34-01 standard [32] . The EXCO test solution was prepared as follows as 4 mol/L NaCl + 0.5 mol/L KNO$_3$ + 0.1 mol/L HNO$_3$ at pH 0.4 in 25°C.

2.2. Electrochemical analysis

The employed electrochemical analyses included open

circuit potential (OCP), potentiodynamic polarization curve, and electrochemical impedance spectroscopy (EIS). Electrochemical measurements were carried out on a conventional three-electrode electrolyte cell system with a platinum electrode as the auxiliary electrode and a saturated calomel electrode (SCE) as the reference electrode. The working electrodes were the weld nugget, the thermo-mechanically affected zone (TMAZ)/heat affected zone (HAZ), and the parent regions across the cross section of the joint. All measurements were carried out in EXCO solution at room temperature. The area of the exposed surface was 0.35 cm^2, and it was polished to a 1-µm diamond finish. For OCP, all electrochemical measurements were performed after immersion in EXCO solution for 30 min to ensure that the working electrodes reached a steady potential in solution. The potentiodynamic polarization curves were then measured at a scanning rate of 1 mV/s. Impedance measurements were carried out over the frequency range of 100 kHz to 10 mHz with a sine wave excitation amplitude of 10 mV at the open circuit potential. The experimental data were analyzed by the commercial software ZSimpWin.

2.3. Immersion tests

The FSW specimens were immersed in EXCO solution for 6 h at 25°C and subsequently treated with the concentrated HNO$_3$ (70vol%) for 30 s. The surface along the cross section of specimens was then cleaned with the distilled water and dried for SEM observation. The exfoliation depth on the top surface of BM was measured under optical microscope using statistical methods.

2.4. *In-situ* observation

All samples were polished to a mirror finish (1-µm diamond paste), ultrasonically cleaned in alcohol, and rinsed in deionized water. Inclusion sites were then identified and marked using a Vickers microhardness tester at the different regions of weld as well as the base metal to identify the intermetallic particles of interest. Subsequently, the marked specimen was immersed in EXCO solution for different periods of time (0.5 h, 1 h, and 2 h). After immersion, the samples were washed in deionized water, dried, and then analyzed by SEM and EDS.

3. Results and discussion

3.1. Identification of intermetallic particles

The macrostructure along the cross section of an FSW joint of 2A14-T6 aluminum alloy is shown in Fig. 1. It can be divided into four regions: weld nugget zone (WNZ),

thermo-mechanically affected zone (TMAZ), heat-affected zone (HAZ), and base material (BM). EDS was used to classify the intermetallic particles of the friction-stir-welded 2A14 aluminum alloy in this experiment. Fig. 2 shows the SEM micrograph of the intermetallic particles in the base material; there are two general particle shapes: round (rod) and irregular. The irregularly-shaped particles (typical greater than 10 μm in length) are much larger than the round ones, which are less than 5 μm in diameter. The EDS spectra from three points (B, D, and H) are shown in Fig. 3. EDS spectrum of the intermetallic particle (point B) shows the elements Al, Cu, Fe, Mn, and Si. The intensity of Al peak is high, and those of Cu, Fe, Mn, and Si peaks are low. The EDS spectrum of point D in Fig. 3(b) shows the high-intensity Al and Cu peaks. Fig. 3(c) displays the representative EDS spectrum of the matrix with a high intensity Al peak and a low intensity Cu peak. The difference in Cu content between the intermetallic particles and the matrix, which results in different corrosion potentials, is considered to be the key factor responsible for the variable corrosion behaviors of FSW joints [26] .

Fig. 4 shows the EDS maps of Fig. 2. The maps indicate a high intensity of Al over the matrix and a low intensity of Al on the precipitate particles. The accumulation of Fe, Mn, and Si is apparent on the particles labeled as B, C, E, and F,
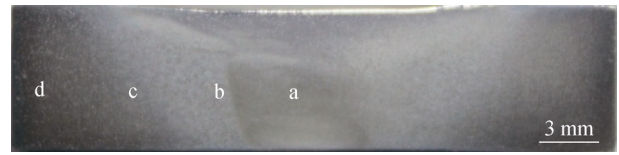

Fig. 1. **Macroscopic image along the cross section of a friction-stir-welded joint of 2A14-T6 aluminum alloy: (a) WNZ; (b) TMAZ; (c) HAZ; (d) BM.**
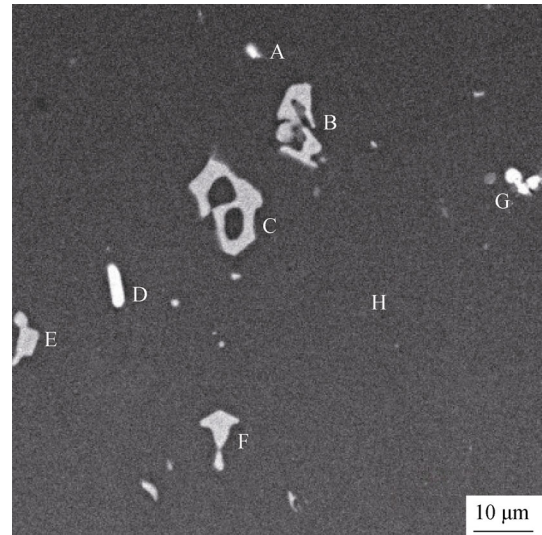

Fig. 2. **SEM image of intermetallic particles in the base material of a friction-stir-welded joint of 2A14-T6 aluminum alloy.**
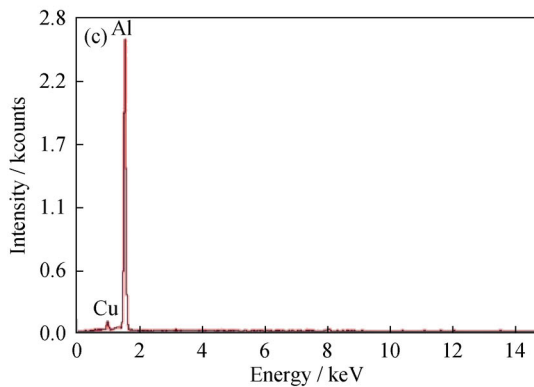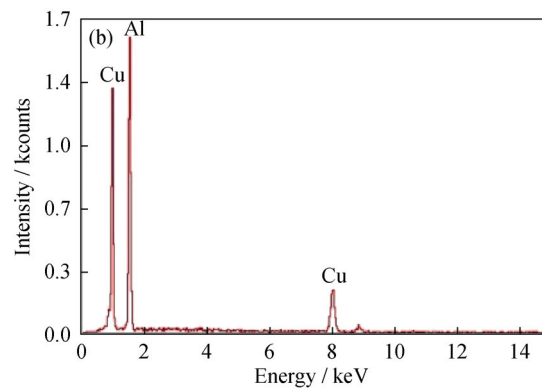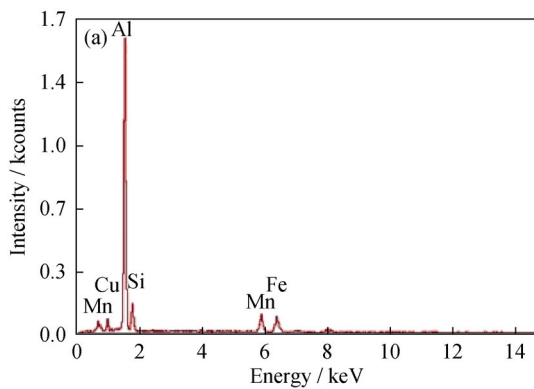

Fig. 3. **EDS spectra from three points in BM in Fig. 2: (a) point B; (b) point D; (c) point H.**
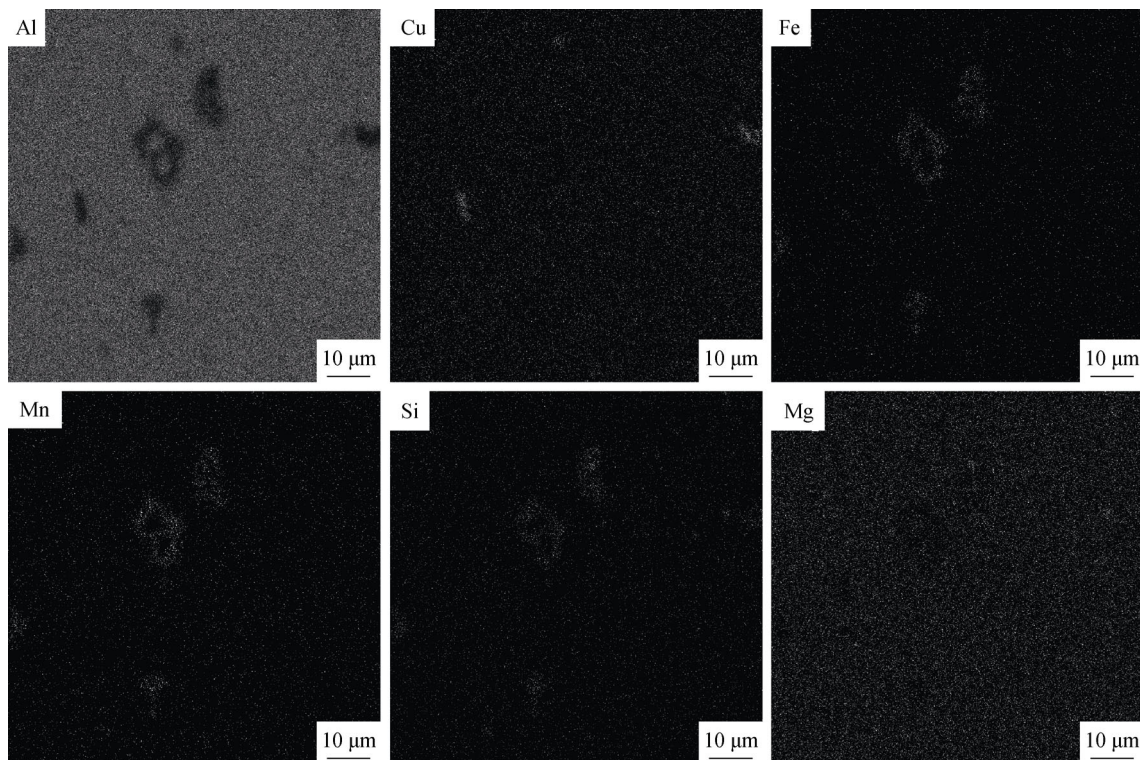
Fig. 4.   EDS maps of the base material of 2A14 aluminum alloy in Fig. 2.

while the intensity of Cu is high on the particles labeled as A, D, and G in Fig. 2. Combined with the results of EDS point analysis, it is easy to identify two typical types of particles: the Al–Cu–Fe–Mn–Si phase (labeled as B, C, E, and F) and the θ phase (labeled as A, D, and G). The intensity of Mg is low for all the intermetallic particles, and no S (Al$_2$CuMg)-phase particles are found under the present conditions.

The SEM image and EDS maps of the particles in the weld nugget of friction-stir-welded joints of 2A14 aluminum alloy are shown in Figs. 5 and 6, respectively. The WNZ is marked by a number of particles. The EDS results for the weld nugget suggest large amounts of Al–Cu–Fe–Mn–Si-phase and θ-phase particles in the joints, in agreement with the results shown in Fig. 4. However, the intensity of Si is large over most of the intermetallic particles due to the stir process, and Mg accumulates on some of the intermetallic particles; thus, other types of precipitates such as Al–Cu–Mg–Si and Al–Cu–Mg may exist in the joints, which may also affect corrosion performance.

3.2. Local electrochemical measurements

The local electrochemical open circuit potentials (E_{OCP}) of the BM, TMAZ/HAZ, and WNZ regions in EXCO solution at 25°C are shown in Fig. 7. For each zone, the OCP measurement was recorded for 400 s. Fig. 7 shows that the potential remains stable in the entire measurement process

for all electrodes, indicating that homogeneous surface corrosion reactivity occurs in the samples [8] . The parent alloy exhibits a potential of around –0.713 V vs. SCE, while those of the TMAZ/HAZ and weld nugget regions are –0.663 V vs. SCE and –0.66 V vs. SCE, respectively. The potentials of the weld nugget and TMAZ/HAZ regions are close, although the weld nugget has a slightly better corrosion resistance, as indicated by its nobler potential.
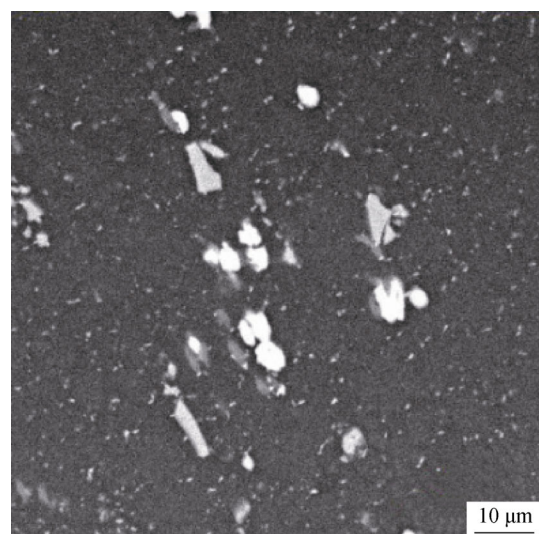

Fig. 5.   SEM image of precipitate particles in the WNZ of the joint of the friction-stir-welded 2A14 aluminum alloy.
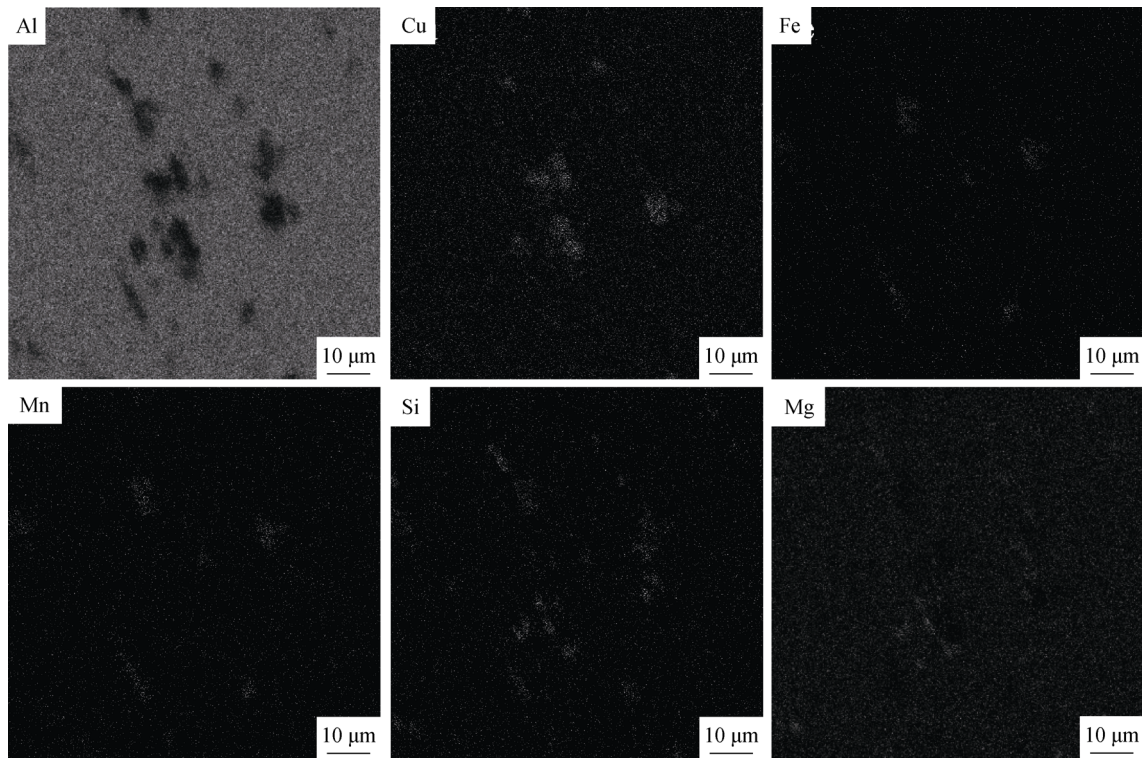
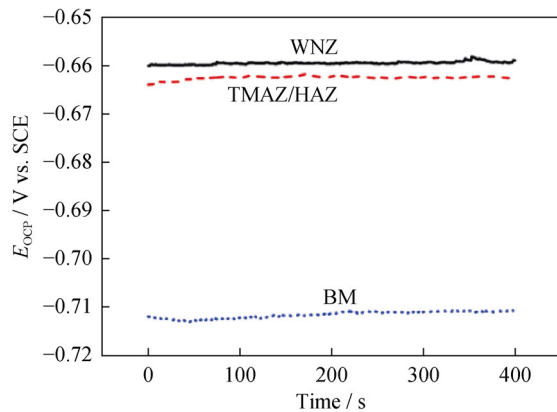**Fig. 6.   WNZ EDS maps of the friction-stir-welded 2A14 aluminum alloy in Fig. 5.**

Fig. 7.   Open circuit potentials of the welded joint at different positions in EXCO solution.

Fig. 8.   Potentiodynamic polarization curves of the joints at different positions in EXCO solution.

Fig. 8 shows the potentiodynamic polarization curves for the 2A14 aluminum alloy joints in EXCO solution. The self-corrosion potentials and self-corrosion currents obtained from Fig. 8 are shown in Table 2. The E_{corr} values of WNZ and TMAZ/HAZ zones are higher than that of BM, and the E_{corr} value of WNZ is the highest. Higher E_{corr} values indicate better corrosion resistance. This result is mainly because the welding area undergoes the significant plastic deformation and recrystallization in the process of FSW, resulting in the microstructural homogenization. The homogenization of microstructure weakens the possibility for the formation of galvanic corrosion, resulting in the improved corrosion resistance.
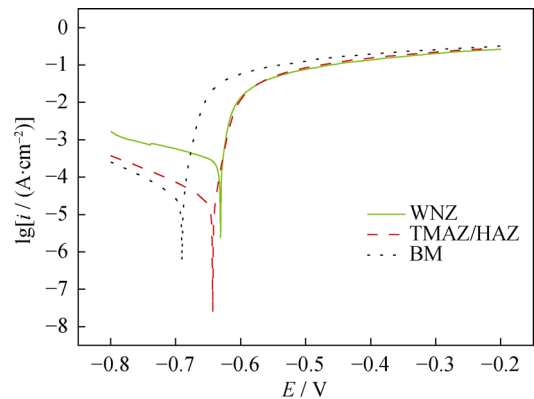
EIS data for the 2A14 aluminum alloy joints in EXCO solution are shown in Fig. 9. The corrosion rate is closely related to the diameter of the capacitive impedance loop, with a larger diameter corresponding to the better corrosion resistance. Fig. 9(a) shows that the diameter of the capacitive impedance loop of WNZ is larger than that of BM, indicating that the corrosion resistance of WNZ is improved compared to BM. The Nyquist plots shown in Fig. 9(a) are all composed of a high-intermediate-frequency capacitive impedance loop and a low-intermediate-frequency inductance loop without a diffusion-controlled linear part; this indicates that the exfoliation corrosion of 2A14 aluminum alloy joints is a charge-transfer-controlled process. Fig. 9 re-

veals that the resistor and capacitor elements are related by the load connection, and the equivalent electric circuit is shown in Fig. 10, where R_Ω stands for the resistance of solution, R_d the charge transfer resistance of the electrochemical reaction, C_d the electric double layer capacitance of electrode/solution, R_f the adsorption resistance of the corrosion production film, and L the induction of the absorbed corrosion production film. To improve the accuracy of fitting, the constant phase angle element (CPE) was used in the place of capacitance to describe the deviation of the capacitance parameter, which was composed of Y_0 and n. The parameter derived from the EIS data was calculated by ZSimpWin software, as listed in Table 2. The R_d and R_f values of WNZ are higher than those of other zones, indicating a lower corrosion rate corresponding to the principal shown in the Nyquist plots in Fig. 9(a).

Table 2. Electrochemical parameters of the joints

Regions	E_{corr} / V	R_Ω / ($\Omega\cdot cm^2$)	Y_0 / ($10^{-5}\Omega^{-1}\cdot cm^2\cdot s^{-n}$)	n	R_d / ($\Omega\cdot cm^2$)	R_f / ($\Omega\cdot cm^2$)
WNZ	−0.631	1.347	1.549	0.9361	1574	16050
TMAZ/HAZ	−0.643	1.402	2.241	0.9517	783.6	5744
BM	−0.690	1.419	1.097	0.9787	303.5	1453

Note: E_{corr} is the self-corrosion potential, R_Ω the resistance of solution, R_d the charge transfer resistance of the electrochemical reaction, and R_f the adsorption resistance of the corrosion production film. Y_0 and n are used to describe the capacitance parameter deviation.
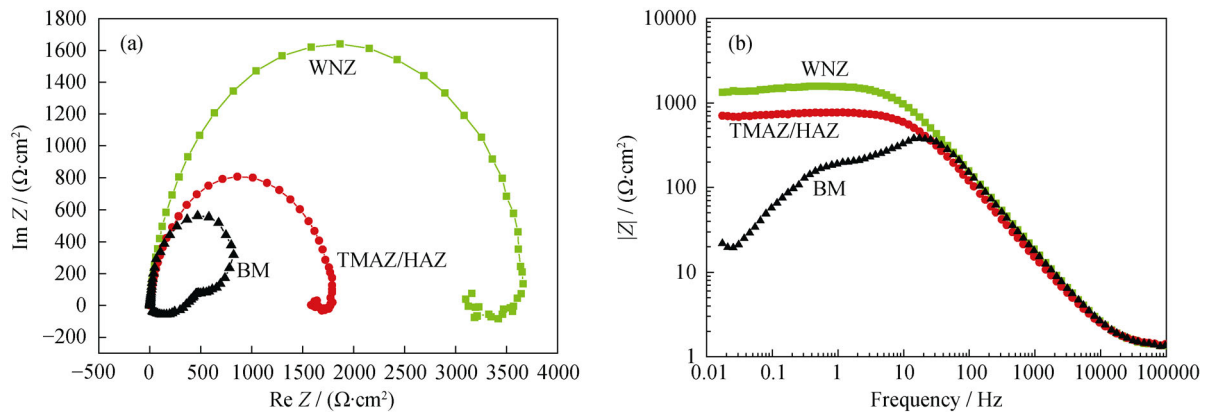

Fig. 9. EIS results of the joints at different positions in EXCO solution: (a) Nyquist plots; (b) Bode plots.
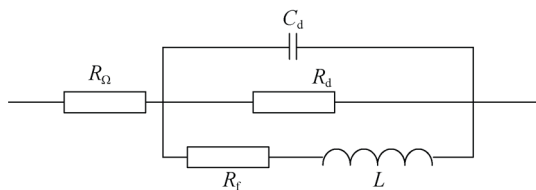

Fig. 10. Equivalent electric circuit used for numerical fitting of the EIS data.

3.3. Corrosion morphology

Fig. 11 shows the macroscopic image of the top surface of the joint after immersion in EXCO solution for 6 h. The major corrosion-affected region is the BM; the exfoliation corrosion is observed with a mean exfoliation depth of 0.13 mm, as shown in Fig. 12. The weld does not suffer from the serious attack, indicating that the weld has higher corrosion resistance than the BM. This result is consistent with the local electrochemical results discussed above.

Some studies have revealed that the exfoliation corrosion sensitivity of aluminum alloy is closely related to the grain aspect ratio, and the mid-section of plate is the most advanced attack place [33] . When intergranular corrosion occurs in a layered structure, the volume of the insoluble corrosion products is larger than that of the aluminum alloy, resulting in a "wedging effect." Therefore, the exfoliation corrosion occurs, causing great losses of surface material [34] . After FSW, the microstructure transforms from elongated grains into a fine and equiaxed grain structure, as shown in Fig. 13; thus, the exfoliation corrosion resistance of friction-stir welds is greatly improved.

Fig. 11. Macroscopic image of the top surface of the joint after immersion in EXCO solution for 6 h.
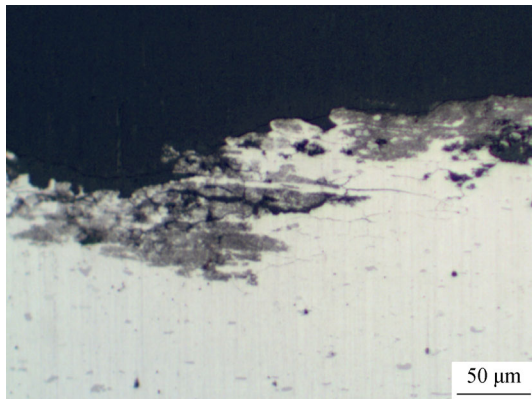
Fig. 12. Exfoliation depth on the top surface of the base material.

The SEM images of the WNZ and the BM zones along the cross section of the joint after immersion tests are shown in Fig. 14. In WNZ, the main type of corrosion attack is pitting corrosion; some pitting holes are detected, and the surface of specimen is smooth. In BM, many corrosion products are found, and some intergranular corrosion is observed. In addition, corrosion pits appear on the BM surface.

3.4. *In-situ* analysis of corrosion behavior

Fig. 15 shows SEM micrographs of the corrosion features of the FSW joint after different immersion times in EXCO solution. Comparing the images in a row, each micrograph represents one state of *in-situ* corrosion for the second phase particles during the corrosion process. After immersion in EXCO solution for 0.5 h, localized pitting corrosion is observed in every region of the joint. The pitting corrosion is first concentrated at the interface between the precipitated phase particles and their adjacent aluminum matrix. This can be attributed to the higher electrode potential of the precipitation phase which contains Cu and Fe with high electrode potentials compared to the aluminum matrix. The second phases with high electrode potentials play the role of cathode, while the aluminum matrix with lower electrode potential is the anode, and dissolution occurs. This observation is in good agreement with the results of other researchers [30] . When immersion time increases to 1 h, some of the second phase particles are also corroded. As a result, these particles become smaller and smaller, indicating that the Al in second phase particles dissolves continuously during the corrosion process. When immersion time reaches 2 h, pitting holes distribute in every region with the formation of new pitting holes as a result of the dissolution of small particles. However, pitting corrosion does not take place in all precipitate particles; only some of the particles dissolve
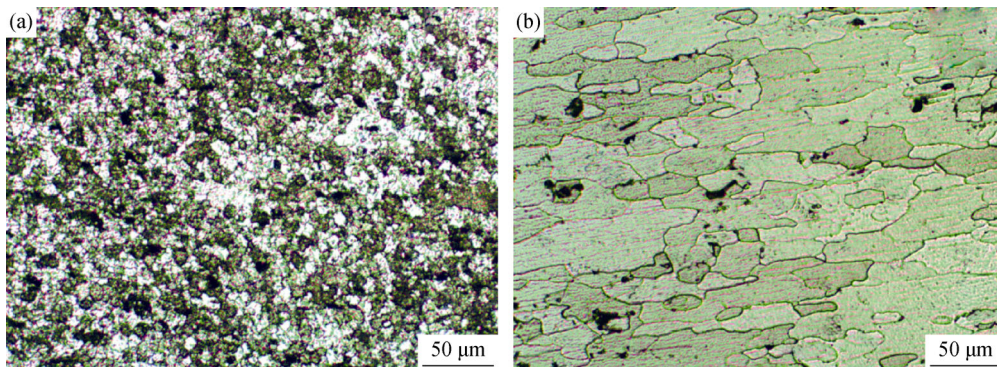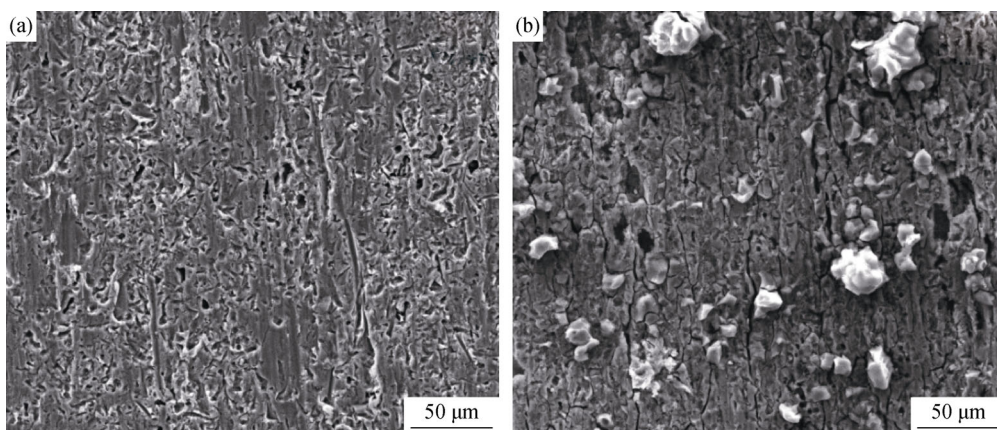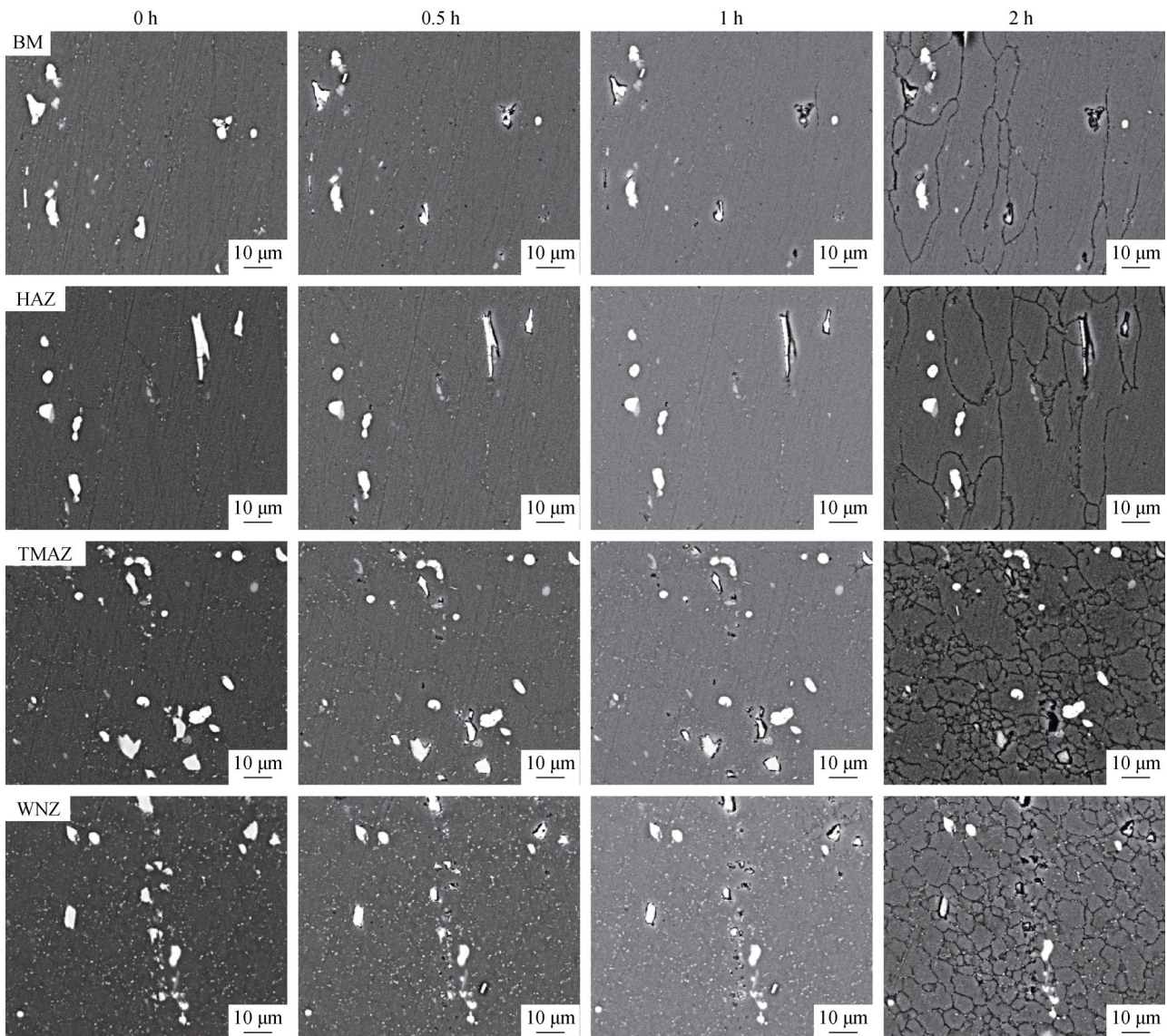

Fig. 13. Optical micrographs of the WNZ (a) and BM (b) zones.

Fig. 14. SEM images of the WNZ (a) and BM (b) zones along the cross section of the joint after immersion in EXCO for 6 h.

Fig. 15.   **Corrosion behavior in the different regions of the FSW joints for different immersion times (0 h, 0.5 h, 1 h, and 2 h) in EXCO solution.**

during EXCO testing. Intergranular corrosion is found in every region after 2 h of exposure to EXCO solution. The intergranular corrosion is generally attributed to the microstructure and element heterogeneity of the grain boundaries resulting from the precipitation of second phase particles at the grain boundaries. This depletes the adjacent solid solution of Cu and makes the adjacent matrix more anodic; therefore, intergranular corrosion is found in the matrix in friction-stir welds. The intergranular corrosion may also be associated with the energy stored in the grains of alloy, as reported by Luo for the AA2024-T351 alloy [35] . These intergranular corrosion phenomena demonstrate that both FSW and BM of 2A14-T6 aluminum alloy are susceptible to intergranular corrosion in EXCO solution.

As shown in Figs. 5 and 15, some precipitate particles are

broken during the FSW process in the weld nugget. They are uniformly distributed on the aluminum matrix due to the rotation of tool. In addition, the microstructure becomes homogeneous in WNZ owing to the significant plastic deformation and recrystallization during the FSW process; the grains are fine and equiaxed, and their sizes are much smaller than those in BM. Consequently, the potential of the galvanic cell between precipitation particles and the Al matrix decreases due to the homogeneous organization and composition. As a result, the weld nugget shows the higher corrosion resistance.

A further investigation into the corrosion behaviors of the two typical precipitate particle phases in BM is shown in Fig. 16. The particle labeled as A is θ phase, while the one labeled as B is Al–Cu–Fe–Mn–Si phase. After immersion in

EXCO solution for 0.5 h, the edge of Al–Cu–Fe–Mn–Si phase particles starts to dissolve. After immersion for 2 h, the Al–Cu–Fe–Mn–Si phase is seriously attacked, while the θ phase particle remains fairy intact without the appearance of pitting corrosion around it. Table 3 shows the contents of Al, Cu, Fe, Mn, and Si in the Al–Cu–Fe–Mn–Si phase particles shown in Fig. 16 before and after immersion in EXCO solution. The element contents in the particles vary with immersion time. With increasing immersion time, the con-

tents of Al and Fe are reduced, while the Cu content increases. After immersion for 2 h, the deposition of O elements is observed on the surface of particles. The EDS data suggest that both the Al–Cu–Fe–Mn–Si phase particles and the aluminum matrix suffer from the corrosion attack. Al and Fe selectively dissolve from the particles, resulting in a Cu-rich remnant. Consequently, the self-corrosion potential of particles increases, and more serious corrosion occurs beside them.
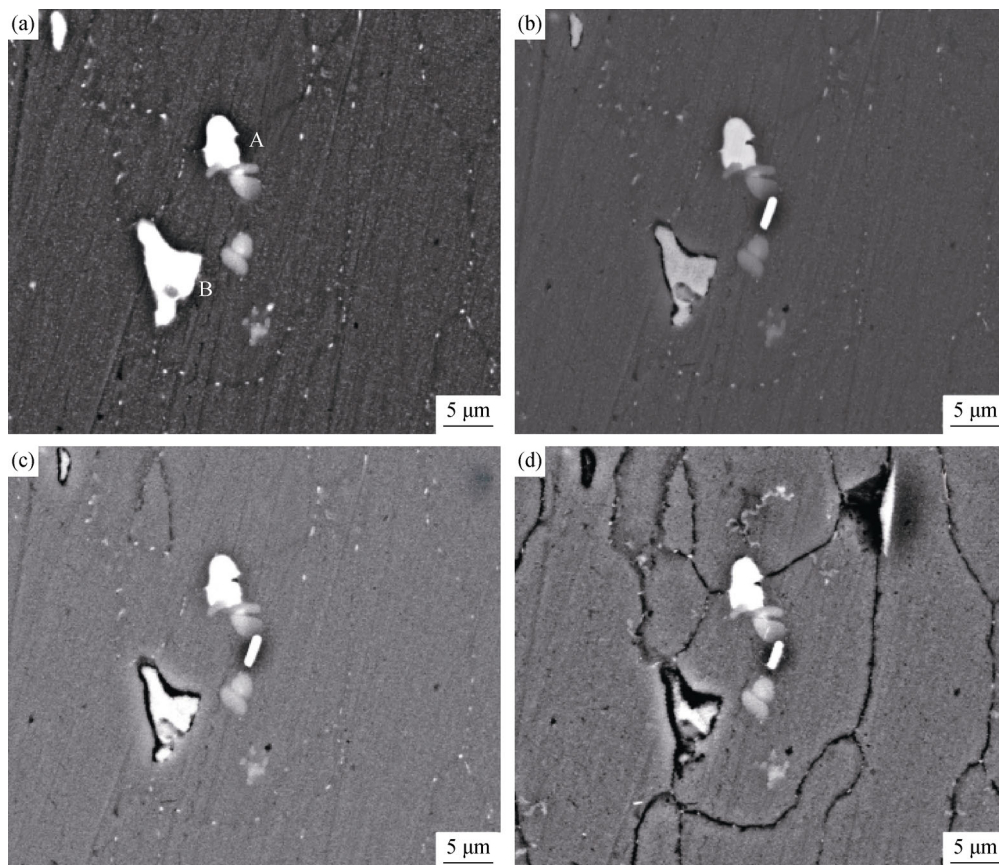

Fig. 16.   Corrosion behavior of precipitate phases in the BM: (a) before immersion; (b) after immersion for 0.5 h; (c) after immersion for 1 h; and (d) after immersion for 2 h.

Table 3.   Composition of Al–Cu–Fe–Mn–Si particles in Fig. 16 with increasing EXCO immersion time   wt%

Immersion time / h	Al	Cu	Fe	Mn	Si	O
Before immersion	59.27	7.07	11.65	13.25	8.76	—
0.5	58.50	8.90	10.65	13.07	8.88	—
1	55.80	11.58	10.63	13.39	8.60	—
2	54.85	13.74	9.20	11.17	6.90	4.14

As previously discussed, there is no observable pitting corrosion either on the θ-phase particles or on the matrix around it in BM. However, two major corrosion types are observed on the Al–Cu–Fe–Mn–Si phase particles. These

particles are reasonably expected to be local cathodes, however, the Al–Cu–Fe–Mn–Si particles also exhibit serious dissolution after immersing for 2 h. Based on this result, another two particles in HAZ are discussed in Fig. 17. The round particle (labeled as A) is θ phase, while the irregularly shaped particle (labeled as B) is Al–Cu–Fe–Mn–Si phase. Fig. 17(a) shows that the size of the Al–Cu–Fe–Mn–Si particle is bigger than that of the previous one in the BM. This is because the HAZ undergoes only high temperature; thus, its grain size is slightly bigger than that in the BM, and the sizes of second phase particles increase at the same time. After immersion in EXCO solution, the Al–Cu–Fe–Mn–Si

phase particle becomes smaller and smaller and is covered by the corrosion products after 2 h, as shown by the EDS spectrum in Fig. 18. However, the θ-phase particle is still

intact after 2 h of immersion, which also supports that the pitting is concentrated only at the Al matrix adjacent to the Al–Cu–Fe–Mn–Si phase particles in HAZ.
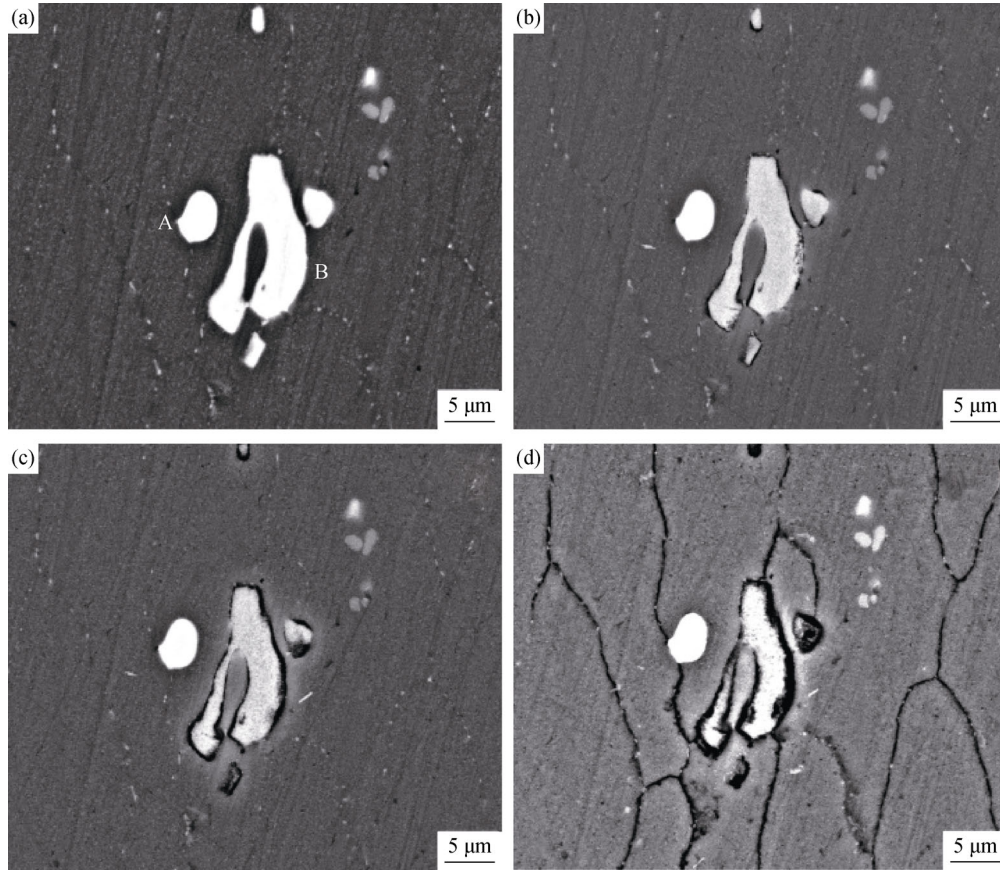

Fig. 17.   Corrosion behavior of precipitates in HAZ: (a) before immersion; (b) after immersion for 0.5 h; (c) after immersion for 1 h; (d) after immersion for 2 h.
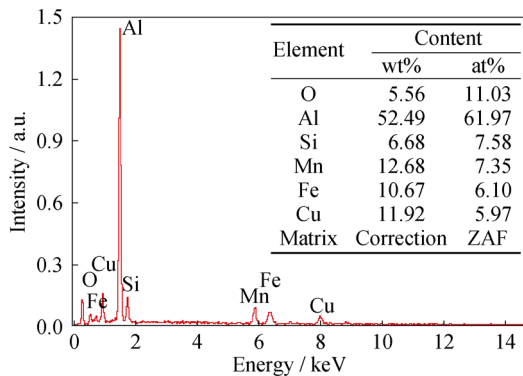

Element	Content	
	wt%	at%
O	5.56	11.03
Al	52.49	61.97
Si	6.68	7.58
Mn	12.68	7.35
Fe	10.67	6.10
Cu	11.92	5.97
Matrix	Correction	ZAF

Fig. 18.   EDS spectrum of Al–Cu–Fe–Mn–Si particle after immersion for 2 h in EXCO solution.

From the analysis above, it can be concluded that the pitting susceptibilities of the FSW joints of 2A14 aluminum alloy are related to the Al–Cu–Fe–Mn–Si particles; some corrosion attacks of the Al–Cu–Fe–Mn–Si particles occur together with the matrix. The EXCO solution is acidic and contains many aggressive ions such as Cl^-, H^+, and NO_3^-.

The oxidation films of particles and the matrix are generally considered to suffer continuously from corrosion attack under the effect of H^+ and Cl^- with increasing immersion time, resulting in the dissolution of aluminum ions followed by their release into solution. However, the effect of NO_3^- on the corrosion behavior of 2A14 aluminum alloy has not been reported, some studies have revealed that NO_3^- can accelerate the dissolution of Fe [36] . While the H^+ in EXCO solution promotes corrosion [34,36]. Therefore, the Al–Cu–Fe–Mn–Si phase in EXCO solution dissolves quickly even though its corrosion potential is much higher than that of the aluminum alloy matrix. The cathodic reaction in EXCO solution is a hydrogen evolution reaction.

4. Conclusions

The corrosion behavior of the friction-stir-welded joints of 2A14-T6 aluminum alloy was investigated and discussed by electrochemical measurements, SEM observations, and

EDS analysis. Based on the results obtained in this study, the following conclusions are summarized.

(1) Two typical phases of precipitate particles are identified in the joints, θ phase and Al–Cu–Fe–Mn–Si phase. The sizes of these particles vary in different regions of the friction-stir-welded joints.

(2) Compared to the base material of 2A14 aluminum alloy, the friction-stir weld is more resistant to exfoliation corrosion, and the weld nugget has the highest corrosion resistance. The friction-stir welds are susceptible to intergranular corrosion in EXCO solution.

(3) The pitting susceptibility is related to the Al–Cu–Fe–Mn–Si phase particles as the cathodes with respect to the matrix due to their high self-corrosion potential, and the pitting corrosion concentrates at the Al matrix adjacent to the particles during the first 0.5 h of immersion in EXCO solution. When immersion time is increased to 2 h, the Al–Fe–Cu–Mn–Si phase is also seriously attacked.

(4) No corrosion activity is observed around the θ phase after 2 h of immersion in EXCO solution.

Acknowledgements

References

[1] R.S. Mishra and Z.Y. Ma, Friction stir welding and processing, *Mater. Sci. Eng. R*, 50(2005), p. 1.

[2] M. Ericsson and R. Sandström, Influence of welding speed on the fatigue of friction stir welds, and comparison with MIG and TIG, *Int. J. Fatigue*, 25(2003), No. 12, p. 1379.

[3] A. Squillace, A. De Fenzo, G. Giorleo, and F. Bellucci, A comparison between FSW and TIG welding techniques: modifications of microstructure and pitting corrosion resistance in AA 2024-T3 butt joints, *J. Mater. Process. Technol.*, 152(2004), No. 1, p. 97.

[4] Y.H. Yau, A. Hussain, R.K. Lalwani, H.K. Chan, and N. Hakimi, Temperature distribution study during the friction stir welding process of Al2024-T3 aluminum alloy, *Int. J. Miner.*

[5] M.J. Jones, P. Heurtier, C. Desrayaud, F. Montheillet, D. Allehaux, and J.H. Driver, Correlation between microstructure and microhardness in a friction stir welded 2024 aluminium alloy, *Scripta Mater.*, 52(2005), No. 8, p. 693.

[6] C.S. Paglia and R.G. Buchheit, A look in the corrosion of aluminium alloy friction stir welds, *Scripta Mater.*, 58(2008), No. 5, p. 383.

[7] R.W. Fonda, P.S. Pao, H.N. Jones, C.R. Feng, B.J. Connolly, and A.J. Davenport, Microstructure, mechanical properties, and corrosion of friction stir welded Al 5456, *Mater. Sci. Eng. A*, 519(2009), No. 1-2, p. 1.

[8] S.M. Li, Y.D. Li, Y. Zhang, J.H. Liu, and M. Yu, Effect of intermetallic phases on the anodic oxidation and corrosion of 5A06 aluminum alloy, *Int. J. Miner. Metall. Mater.*, 22 (2015), p. 167.

[9] E. Bousquet, A. Poulon-Quintin, M. Puiggali, O. Devos, and M. Touzet, Relationship between microstructure, microhardness and corrosion sensitivity of an AA 2024-T3 friction stir welded joint, *Corros. Sci.*, 53(2011), No. 9, p. 3026.

[10] V. Fahimpour, S.K. Sadrnezhaad, and F. Karimzadeh, Corrosion behavior of aluminum 6061 alloy joined by friction stir welding and gas tungsten arc welding methods, *Mater. Des.*, 39(2012), p. 329.

[11] J. Kang, R.D. Fu, G.H. Luan, C.L. Dong, and M. He, *In-situ* investigation on the pitting corrosion behavior of friction stir welded joint of AA2024-T3 aluminium alloy, *Corros. Sci.*, 52(2010), p. 620.

[12] W.F. Xu, J.H. Liu, and H.Q. Zhu, Pitting corrosion of friction stir welded aluminium alloy thick plate in alkaline chloride solution, *Electrochim. Acta*, 55(2010), No. 8, p. 2918.

[13] W.F. Xu and J.H. Liu, Microstructure and pitting corrosion of friction stir welded joints in 2219-O aluminum alloy thick plate, *Corros. Sci.*, 51(2009), No. 11, p. 2743.

[14] V. Proton, J. Alexis, E. Andrieua, J. Delfossec, M.C. Lafonta, and C. Blanc, Characterisation and understanding of the corrosion behaviour of the nugget in a 2050 aluminium alloy friction stir welding joint, *Corros. Sci.*, 73(2013), p. 130.

[15] T.H. Tra, M. Okazaki, and K. Suzuki, Fatigue crack propagation behavior in friction stir welding of AA6063-T5: roles of residual stress and microstructure, *Int. J. Fatigue.*, 43(2012), p. 23.

[16] P. Bala Srinivasan, W. Dietzel, R. Zettler, J.F. dos Santos, and V. Sivan, Stress corrosion cracking susceptibility of friction stir welded AA7075-AA6056 dissimilar joint, *Mater. Sci. Eng. A*, 392(2005), No. 1-2, p. 292.

[17] H.B. Li, Z.H. Jiang, H. Feng, H.C. Zhu, B.H. Sun, and Z. Li, Corrosion behavior of ferritic stainless steel with 15wt% chromium for the automobile exhaust system, *Int. J. Miner. Metall. Mater.*, 20(2013), p. 850.

[18] Y. Yang and L.L. Zhou, Improving corrosion resistance of friction stir welding joint of 7075 aluminum alloy by micro-arc oxidation, *J. Mater. Sci. Technol.*, 30(2014), No. 12, p. 1251.

[19] M. Jariyaboon, A.J. Davenport, R. Ambat, B.J. Connolly,

Metall. Mater., 20(2013), p. 779.

S.W. Williams, and D.A. Price, Effect of cryogenic cooling on corrosion of friction stir welded AA7010-T7651, *Anti-Corros. Methods Mater.*, 57(2010), No. 2, p. 83.

[20] C. Padovani, A.J. Davenport, B.J. Connolly, S.W. Williams, E. Siggs, A. Groso, and M. Stampanoni, Corrosion protection of AA7449-T7951 friction stir welds by laser surface melting with an Excimer laser, *Corros. Sci.*, 53(2011), No. 12, p. 3956.

[21] S.J. Kalita, Microstructure and corrosion properties of diode laser melted friction stir weld of aluminum alloy 2024 T351, *Appl. Surf. Sci.*, 257(2011), No. 9, p. 3985.

[22] O. Hatamleh, P.M. Singh, and H. Garmestani, Corrosion susceptibility of peened friction stir welded 7075 aluminum alloy joints, *Corros. Sci.*, 51(2009), No. 1, p. 135.

[23] K. Prasad Rao, G.D. Janaki Ram, and B.E. Stucker, Improvement in corrosion resistance of friction stir welded aluminum alloys with micro arc oxidation coatings, *Scripta Mater.*, 58(2008), No. 11, p. 998.

[24] K. Surekha, B.S. Murty, and K. Prasad Rao, Microstructural characterization and corrosion behavior of multipass friction stir processed AA2219 aluminium alloy, *Surf. Coat. Technol.*, 202(2008), No. 17, p. 4057.

[25] K. Surekha, B.S. Murty, and K. Prasad Rao, Effect of processing parameters on the corrosion behaviour of friction stir processed AA 2219 aluminum alloy, *Solid State Sci.*, 11(2009), No. 4, p. 907.

[26] K. Surekha, B.S. Murty, and K. Prasad Rao, Comparison of corrosion behaviour of friction stir processed and laser melted AA 2219 aluminium alloy, *Mater. Des.*, 32(2011), No. 8-9, p. 4502.

[27] Z. Liu, P.H. Chong, A.N. Butt, P. Skeldon, and G.E. Thompson, Corrosion mechanism of laser-melted AA 2014 and AA 2024 alloys, *Appl. Surf. Sci.*, 247(2005), No. 1-4, p. 294.

[28] C.M. Liao and R.P. Wei, Galvanic coupling of model alloys to aluminum: a foundation for understanding particle-induced pitting in aluminum alloys, *Electrochim. Acta*, 45(1999), No. 6, p. 881.

[29] C. Blanc, A. Freulon, M.C. Lafont, Y. Kihn, and G. Mankowski, Modelling the corrosion behaviour of Al_2CuMg coarse particles in copper-rich aluminium alloys, *Corros. Sci.*, 48(2006), No. 48, p. 3838.

[30] M.H. Shao, Y. Fu, R.G. Hu, and C.J. Lin, A study on pitting corrosion of aluminum alloy 2024-T3 by scanning microreference electrode technique, *Mater. Sci. Eng. A*, 344(2003), No. 1-2, p. 323.

[31] R. Grilli, M.A. Baker, J.E. Castle, B. Dunn, and J.F. Watts, Localized corrosion of a 2219 aluminium alloy exposed to a 3.5% NaCl solution, *Corros. Sci.*, 52(2010), No. 9, p. 2855.

[32] American Society for Testing and Materials, ASTM G34-01, *Standard Test Method for Exfoliation Corrosion Susceptibility in 2XXX and 7XXX Series Aluminum Alloys* (*EXCO Test*), West Conshohocken, Pennsylvania, 2013.

[33] M.J. Robinson and N.C. Jackson, The influence of grain structure and intergranular corrosion rate on exfoliation and stress corrosion cracking of high strength Al–Cu–Mg alloys, *Corros. Sci.*, 41(1999), No. 5, p. 1013.

[34] A. Conde and J. de Damborenea, Evaluation of exfoliation susceptibility by means of the electrochemical impedance spectroscopy, *Corros. Sci.*, 42(2000), p. 1363.

[35] C. Luo, X. Zhou, G.E. Thompson, and A.E. Hughes, Observations of intergranular corrosion in AA2024-T351: the influence of grain stored energy, *Corros. Sci.*, 61(2012), p. 35.

[36] C. Gabrielli, M. Keddam, E. Stupnišek-Lisac, and H. Takenouti, Etude du comportement anodique de l'interface fer-acide nitrique a l'aide d'une regulation a resistance negative, *Electrochim. Acta*, 21(1976), No. 10, p. 757.